

# Excimer laser ablation of single crystal 4H-SiC and 6H-SiC wafers

Saurabh Gupta · Ben Pecholt · Pal Molian

Received: 18 April 2010 / Accepted: 10 September 2010 / Published online: 23 September 2010  
© Springer Science+Business Media, LLC 2010

**Abstract** A 248 nm, 23 ns pulsed excimer laser was used to compare the ablation characteristics of single crystal wafers of the polytypes 4H-SiC and 6H-SiC over a wide range of energy fluence ( $0.8\text{--}25\text{ J cm}^{-2}$ ). Photothermal models based on Beer–Lambert equation using thermal diffusivity and absorption coefficient, energy balance, and heat transfer were presented to predict the ablation mechanisms. Micromachining of trenches was demonstrated at  $7\text{ J cm}^{-2}$  to demonstrate the potential of UV laser ablation. Results indicate that the ablation process is characterized by two well-defined threshold fluences: (a) decomposition threshold  $\sim 1\text{ J cm}^{-2}$  and (b) melting threshold  $\sim 1.5\text{ J cm}^{-2}$  for both polytypes. Contrary to the modeling expectations, the ablation rates were lower and did not increase rapidly with energy fluence. Four types of ablation mechanisms—chemical decomposition, vaporization, explosive boiling, and plasma shielding—either singly or in combination occur as a function of energy fluence. The predictions of photothermal models were not in good agreement with the experimental data implying that a complex interplay among various physical phenomena occurs during ablation. Micromachined trench exhibited ripple patterns, microcracks and recast layers, most of which could be eliminated by a subsequent chemical cleaning process. It is concluded that excimer laser ablation is an effective but slow material removal process for SiC wafers compared to other lasers such as 1064 nm Nd:YAG.

## Introduction

Silicon carbide (SiC) can be used as a semiconductor or insulator in high-temperature and harsh chemical environments due to its exceptional properties such as wide band-gap, chemical inertness, thermal stability, and mechanical strength. SiC finds a number of applications in the fields of power electronics, microelectronics, and micro-electro-mechanical-systems (MEMS). Physical and chemical sensors, micromotors and resonators are some examples of SiC-based MEMS devices that are designed to operate in heat, chemical, and radiation environments [1–3]. High-temperature pressure sensors are particularly attractive for automotive (fuel engines), manufacturing (down-hole drilling operations), energy (petrochemical refineries), and environmental (HVAC systems) applications. A single crystal SiC-based sensor diaphragm with piezoresistors can withstand the dynamic pressure changes encountered in such harsh environments. However, fabrication of such thin diaphragms remains as a formidable challenge.

Amongst 200 or more polytypes of SiC [4], only three types—3C-SiC, 6H-SiC, and 4H-SiC—could be grown in single crystalline form for use in microelectronics and MEMS devices. The rigid process control requirements in the single crystal growth techniques for obtaining defect-free 3C-SiC wafer [5] prevented its commercial availability. On the other hand, single crystalline 4H and 6H wafers are readily available in various sizes (ranging from 50 to 100 mm). Conventional fabrication of 4H and 6H SiC for MEMS applications includes reactive ion etching (RIE), electron cyclotron resonance (ECR), and deep reactive ion etching (DRIE) which suffer from poor etch selectivity, slow etch rates and require the use of masks in the etch field [6, 7]. Laser ablation is emerging as an alternative

S. Gupta · B. Pecholt · P. Molian (✉)  
Department of Mechanical Engineering, Laboratory for Lasers,  
MEMS and Nanotechnology, Iowa State University, Ames,  
IA 50011, USA  
e-mail: molian@iastate.edu

technique, offering a clean, simple, and maskless method with higher etch rates. In fact, etch rates ranging from 0.47 to 1.8  $\mu\text{m pulse}^{-1}$  have been achieved using nanosecond pulsed Nd:YAG lasers on 4H-SiC polytypes [8–10]. SiC has high optical absorption at UV wavelengths [11] and shows nearly linear correlation between the number of pulses and ablation depth [12]; this makes UV lasers as excellent choices for micromachining of SiC-based MEMS devices.

In the nanosecond or longer pulse regime, when the incident photons have sufficient energy to overcome the bandgap, single-photon absorption occurs, which causes the jumping of electrons from the valence band to the conduction band. It may be noted that the photon energy corresponding to 248 nm (5 eV) is much higher than the bandgaps of 4H-SiC (3.26 eV) and 6H-SiC (3.03 eV); this in turn facilitates single-photon absorption through direct electronic interaction with the bandgap of SiC. The excited electrons jump to the conduction band causing a strong increase in phonon energy that leads to the lattice disorder, bond breaking, and subsequent ablation [13]. However, direct bond scission, ionization or atomic emission are not possible in SiC as the minimum energy required to break the bonds, i.e., the sum of electron affinity ( $\sim 4.0$  eV) and bandgap energy ( $\sim 3$  eV), is greater than the energy corresponding to a photon (5 eV) [13, 14]. The bond scission is supposed to be caused by cascade excitation through localized electron states [15].

In this paper, we report the ablation behavior of single crystal 4H-SiC and 6H-SiC wafers when subjected to 23 ns pulsed, 248 nm wavelength excimer laser. The ablation mechanisms were correlated with the energy fluence. Furthermore, the trenches were demonstrated to show the capability of excimer laser micromachining in fabricating sensor diaphragms.

### Experimental details

Single crystalline wafers of the types 4H and 6H (n-type semiconductor, nitrogen dopant density  $\sim 10^{17} \text{ cm}^{-3}$ , silicon face polished/epi ready) with 50 mm diameter and 250  $\mu\text{m}$  thick were procured from Cree, Inc (NC, USA). Table 1 lists the electronic, thermal, and optical properties of these two polytypes relevant to laser micromachining.

A 248 nm (KrF) excimer laser (Lambda Physik Model 110i) was employed to study the ablation characteristics and for micromachining purpose. The specifications of the laser are listed in Table 2.

Figure 1 shows the schematic diagram of beam delivery unit used with the excimer laser system. The large beam was passed through a beam delivery unit consisting of 200  $\times$  100 mm telescope lens, adjustable razorblade aperture, 90° turning mirror and 100 mm image lens. The telescope lenses are arranged in a standard telecentric (afocal) configuration and serve the purpose of increasing the energy density on the aperture by a factor of four. The turning mirror redirects the laser beam to the workpiece. The image lens is used to project the aperture on the workpiece at a given demagnification ratio which is 7 $\times$  in this study. The demagnification,  $M$  is defined as  $M = O/I$  where  $O$  is the distance from the aperture to the image lens and  $I$  is the distance from the image lens to the workpiece.

For ablation studies, the laser pulse energy and repetition rate were varied from 10 to 200 mJ and 1 to 50 Hz, respectively. The spot size was approximately 250  $\times$  100  $\mu\text{m}$ . Consequently the energy fluence was varied between 0.8 and 25  $\text{J cm}^{-2}$ . All experiments were carried out in an atmosphere where  $\text{N}_2$  gas was directly flowing over the exposed surface so that it can mitigate the formation of  $\text{SiO}_2$  caused by the oxidation of SiC surface.

**Table 1** Physical properties of single crystal SiC polytypes

Polytype	4H-SiC	6H-SiC	Reference
Reflectivity at 248 nm	0.26	0.3	[16, 17]
Absorption coefficient at 248 nm ( $\text{m}^{-1}$ )	$6 \times 10^5$	$5 \times 10^6$	[18–20]
Thermal diffusivity, $\text{m}^2 \text{ s}^{-1}$	$1.7 \times 10^{-4}$	$2.2 \times 10^{-4}$	[21]
Thermal conductivity, $\text{W m}^{-1} \text{ K}^{-1}$	370	490	[21]
Density, $\text{kg m}^{-3}$	3200	3200	[22]
Specific heat, $\text{J kg}^{-1} \text{ K}^{-1}$	690	690	[23]

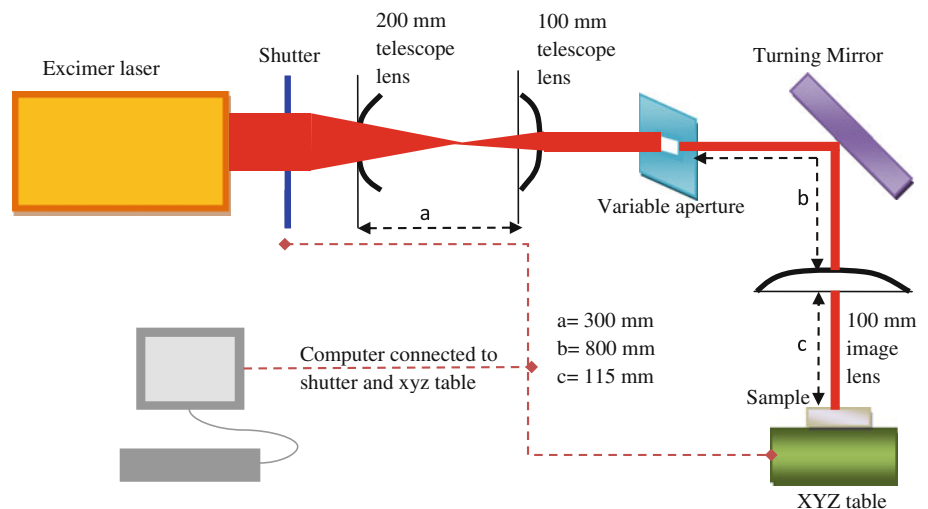
All values taken at 300 K

<sup>a</sup> Interpolated from Ref. [19]

**Table 2** Specifications of laser used in this investigation

Wavelength	Max. pulse energy	Pulse width	Max. repetition rate	Max. average power	Beam size	Beam profile
248 nm	300 mJ	23 ns	100 Hz	30 W	12 $\times$ 23 mm	Multimode

**Fig. 1** A schematic diagram of beam delivery unit used with the excimer laser



Ablation depths and profiles were obtained using a Zygo optical profilometer.

For micromachining trenches, the energy fluence, and repetition rate were set constant at  $7 \text{ J cm}^{-2}$  and 10 Hz, respectively. The spot size on the sample was increased to approximately  $1500 \times 500 \text{ }\mu\text{m}$ . The sample was held stationary with respect to laser beam, thereby reducing the possibility of any ramp features that may occur on the surface due to relative motion of the beam. Following laser micromachining, the samples were cleaned using HCl:H<sub>2</sub>O:H<sub>2</sub>O<sub>2</sub> (1:1:1) for 5 min and then treated with HF:H<sub>2</sub>O (1:1) for 7 min. The samples were examined in scanning electron microscope (SEM) for debris, feature size, and geometry.

## Results and discussion

### Ablation characteristics

Laser ablation of materials in the UV region may be classified as photothermal or photochemical or a combination of both depending on the material's thermal diffusivity, pulse duration, and absorption coefficient. The effects of material characteristics and laser parameters on the ablation rate are presented in the literature [24, 25]. If thermal penetration depth  $L_e = 2(\kappa t)^{1/2}$  is greater than optical absorption depth  $L_o = \alpha^{-1}$ , thermal ablation dominates (where  $t$  is the pulse duration in seconds,  $\kappa$  is the thermal diffusivity, and  $\alpha$  is the absorption coefficient of the material). Otherwise, photochemical ablation governs. Using properties given in Table 1 (300 K),  $L_e$  and  $L_o$  for both polytypes were calculated and listed in Table 3.

The ablation rate (depth of material removed per pulse) was measured for both polytypes using 1 Hz for 50 pulses (Fig. 2). The ablation rate follows initially an exponential

**Table 3** Calculated values of  $L_e$  and  $L_o$  with 248 nm excimer laser at 300 K

Polytype	4H-SiC ( $\mu\text{m}$ )	6H-SiC ( $\mu\text{m}$ )
Thermal penetration depth ( $L_e$ )	$\sim 4$	$\sim 4.5$
Optical absorption depth ( $L_o$ )	$\sim 1.7$	$\sim 0.2$

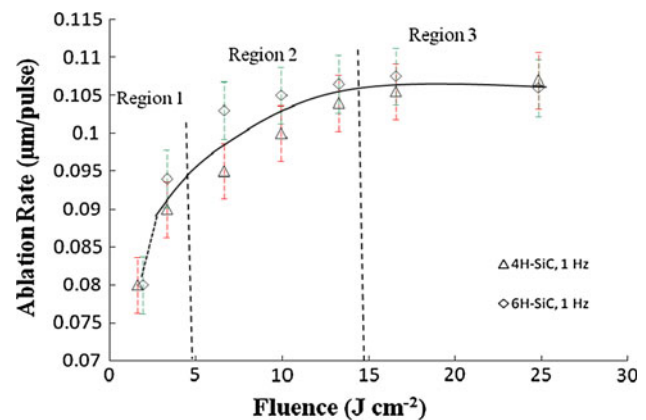
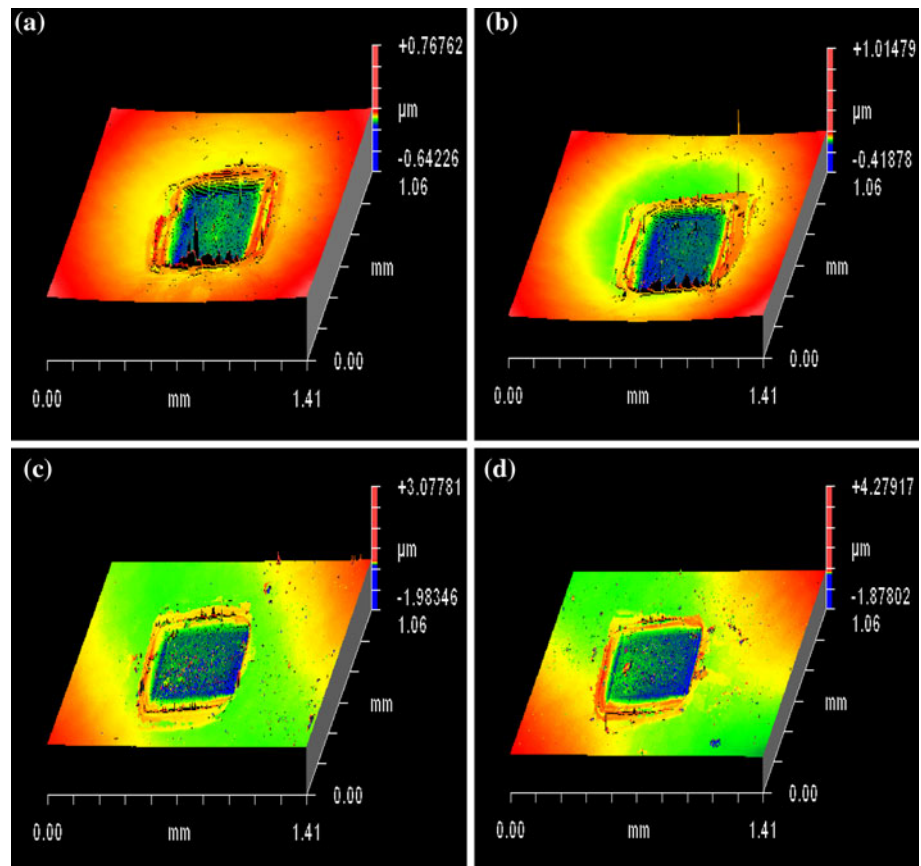


**Fig. 2** Ablation rate as a function of fluence for SiC

curve that agrees well with the previous work by Reitano and Baeri [26] using XeCl excimer laser (308 nm) ablation of 6H-SiC crystals. The ablation rate fluctuated very little above a fluence of  $15 \text{ J cm}^{-2}$ , indicating a saturation point. The ablation curve can be divided into three different regimes based on the changes in slope, indicating possibly a different mechanism in each region.

Figures 3 and 4 show three-dimensional surface maps and depth profiles, respectively, for both polytypes for energy fluencies in Region 1 of Fig. 2. It can be seen that the ablation profile does not change significantly when the fluence was increased from  $0.8$  to  $1.25 \text{ J cm}^{-2}$ . Furthermore, the bottom surface of 6H-SiC was more irregular relative to 4H-SiC (Fig. 4). However, the ablation rate

**Fig. 3** Surface maps for **a** 4H-SiC, 0.85 J cm<sup>-2</sup>; **b** 4H-SiC, 1.24 J cm<sup>-2</sup>; **c** 6H-SiC, 0.85 J cm<sup>-2</sup>; and **d** 6H-SiC, 1.24 J cm<sup>-2</sup>



increases considerably  $\sim 0.01 \mu\text{m pulse}^{-1}$  after a certain threshold. The corresponding fluence was interpolated to be ( $\sim 0.6 \text{ J cm}^{-2}$ ) for 4H-SiC and ( $\sim 0.9 \text{ J cm}^{-2}$ ) for 6H-SiC. A higher bandgap and presence of fewer Si-C bilayers in the unit cell of 4H-SiC are believed to be responsible for its slightly lower threshold fluence than that of 6H-SiC.

The ablation depth as a function of number of pulses was also measured for both polytypes and results are compared as shown in Fig. 5. The ablation rate was found to be linear and nearly identical for both types of SiC. Such linear relationship was also noted in a previous investigation [12] and is in accordance with the single-photon absorption mechanism. The error bars indicate a negative ablation depth which corresponds to surface elevation at low pulses.

We will explore a number of models used to predict the ablation rates and thereby identify the material removal mechanisms. The first model considered is based on heat diffusion that can take place at a time scale much shorter than the pulse duration used in this study [27]. The ablation depth per pulse can be expressed by modifying the Beer-Lambert law (in terms of  $L_c$ ) as [28]:

$$D = 2(\kappa t)^{1/2} \ln \frac{F_i}{F_t} \quad (1)$$

Thermal diffusivity for SiC varies with temperature according to the relation given as  $\kappa = \frac{146}{(T-207)} \text{ cm}^2 \text{ s}^{-1}$  for

$300 < T < 2300 \text{ K}$  [23]. The ablation depth was calculated using Eq. 1, and results were compared with experimental data. The calculated results are substantially higher than the experimental data implying that this model is not valid for the present case. The reasons for the invalidity are: (1) Eq. 1 assumes that the whole diffusion zone is subjected to temperatures higher than the vaporization; (2) Eq. 1 does not take into account the energy losses due to plasma formation and reflection at the surface.

The second model is based on effective absorption which combines absorption and thermal diffusivity. The effective absorption coefficient ( $\alpha_{\text{eff}}$ ) can be defined as [29]:

$$\alpha_{\text{eff}} = [\alpha^{-1} + 2(\kappa t)^{1/2}]^{1/2} \quad (2)$$

Thus, substituting the value of  $\alpha_{\text{eff}}$  in Beer-Lambert equation, the modified expression for ablation depth per pulse can be written as:

$$D = [\alpha^{-1} + 2(\kappa t)^{1/2}]^{1/2} \ln \frac{F_i}{F_t} \quad (3)$$

Obviously this model will not work because the calculated results would be even higher than those obtained in the previous model. However, this model illustrates that the ablation rate will be expected to be higher in 4H-SiC than 6H-SiC due to the differences in absorption coefficient.

**Fig. 4** Depth profiles for **a** 4H-SiC,  $0.85 \text{ J cm}^{-2}$ ; **b** 4H-SiC,  $1.24 \text{ J cm}^{-2}$ ; **c** 6H-SiC,  $0.85 \text{ J cm}^{-2}$ ; and **d** 6H-SiC,  $1.24 \text{ J cm}^{-2}$

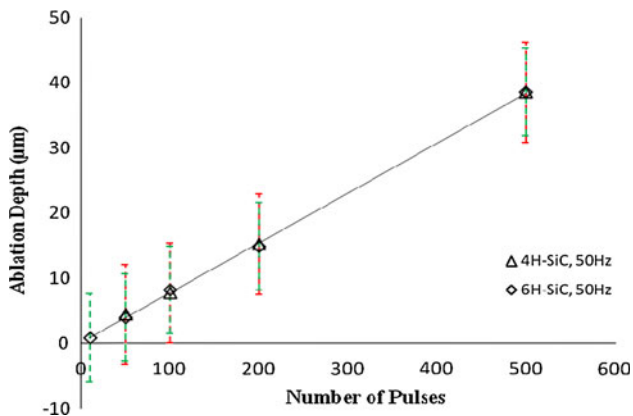
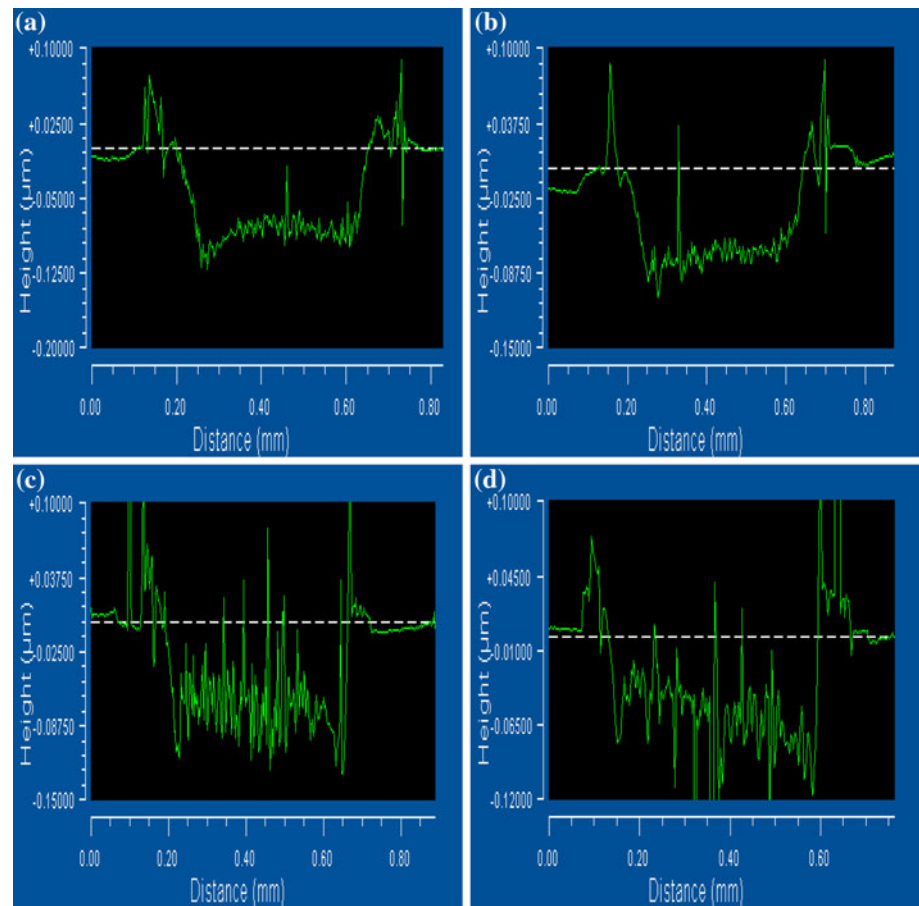


**Fig. 5** Ablation depth vs number of pulses for SiC using  $8 \text{ J cm}^{-2}$  at 50 Hz

In both models, the assumption that the process lasts only as long as the pulse duration leads to the overestimate of ablation rates. Realistically the temperature build up occurs beyond the pulse duration [30]. It has been reported that the rate at which heat is transferred within a material depends on the temperature gradient and thermal conductivity of the material [31–33]. The losses due to heat conduction are

considerable for all materials at all fluences. The absorbed power density can be modeled as the heat flux into the SiC surface and the temperature distribution  $T(x,t)$  can be estimated by solving the heat transfer equation for a semi-infinite solid in one-dimension, written as [34]:

$$T(x,t) = \frac{I_0}{k} \sqrt{\frac{4kt}{\pi}} \times \left( e^{-x^2/4kt} - x \sqrt{\frac{\pi}{4kt}} \operatorname{erfc} \left( \frac{x}{\sqrt{4kt}} \right) \right) \quad (4)$$

where  $I_0$  is absorbed power density at the surface and  $k$  is the thermal conductivity of material.

Equation 4 considers thermal conductivity and diffusivity at room temperature. This is not valid because both thermal conductivity and diffusivity vary with temperature. In order to accommodate this effect, an average value of both the quantities was calculated using the data in Table 1 and the following relationship:  $\kappa = \frac{146}{(T-207)} \text{ cm}^2 \text{ s}^{-1}$  for  $300 < T < 2300 \text{ K}$  and  $k = \frac{611}{(T-115)} \text{ W cm}^{-1} \text{ K}^{-1}$  for  $300 < T < 2300 \text{ K}$  [23]. The results, shown in Fig. 6, indicate a good similarity in the temperature distribution for both polytypes. We now focus on the ablation mechanisms in the three different regimes shown in Fig. 5.



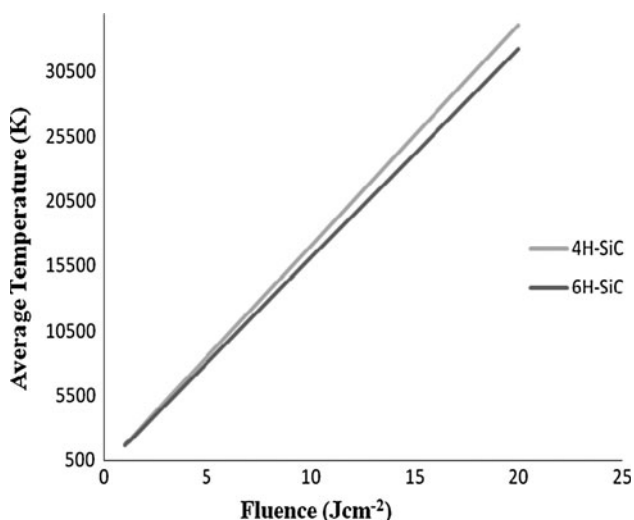


**Fig. 6** Plot showing distribution of average temperature of the ablated zone as a function of fluence based on heat transfer model for both polytypes of SiC

*Region 1 ( $\leq 5 \text{ J cm}^{-2}$ )*

*Decomposition mechanism ( $< 1.25 \text{ J cm}^{-2}$ )* It has been reported that SiC decomposes into silicon gas and solid carbon at temperatures ranging from 1600 to 2400 K, and the carbon may then react further with SiC and silicon gas to form other vapor species such as SiC<sub>2</sub> and Si<sub>2</sub>C [35, 36]. For this temperature range, the fluence range at which decomposition occurs was determined using Fig. 6. The corresponding fluence values are listed in Table 4. The results indicate that SiC decomposes well below a fluence of  $1.25 \text{ J cm}^{-2}$ .

*Vaporization mechanism ( $1.25\text{--}5 \text{ J cm}^{-2}$ )* It is a well known fact that when a high-power laser beam (laser intensity  $\geq 10^8 \text{ W cm}^{-2}$ ) irradiates on a target surface, laser energy is absorbed by the target and vapor is formed. Several models have been reported the vaporization characteristics of semiconductors with nanosecond pulsed lasers [34, 37, 38]. In a study done on silicon melting using a nanosecond pulsed laser, the relaxation time ( $\tau_m$ ) at which melting occurs is given by [38]:

**Table 4** Estimation of fluence range at which SiC decomposes

Fluence ( $\text{J cm}^{-2}$ )	Temperature (K) based on energy balance model <sup>a</sup>	Temperature (K) based on heat transfer model <sup>a</sup>
1	1730	1640
1.1	1920	1835
1.2	2100	1950
1.25	2340	2280

<sup>a</sup> Average temperatures for both polytypes

$$\tau_m = \left( \frac{3(T_m - T_0)^2 c \rho k}{4J_0^2} \right) \tag{5}$$

where  $c$  is the heat capacity,  $\rho$  is the density,  $k$  is the thermal conductivity,  $T_m$  is the melting temperature, and  $T_0$  is the initial temperature of the target material. However, the relaxation time is lower if a shield gas like nitrogen and higher scan rates were used. Using the values given in Table 1 and assuming  $T_m$  for carbon as equal to 4000 K [39, 40],  $\tau_m$  was plotted as a function of fluence (Fig. 7). It can be observed that the decomposition products begin to melt at fairly low fluences as predicted in the previous research [35]. The relaxation time,  $\tau_m$  decreases rapidly with increasing energy fluence. To validate our experimental data,  $\tau_m$  was set equal to the pulse duration time (23 ns) and an approximate melting threshold fluence was determined to be  $\sim 1.5 \text{ J cm}^{-2}$  for both polytypes. It can, therefore, be inferred that the ablation mechanism in Region 1 is primarily driven by melting of carbon followed by vaporization of carbon and silicon species which are formed as a result of SiC decomposition.

To determine the ablation rate in Region 1, we calculate the evaporation rate of the melt under the influence of laser fluence. The evaporation rate  $G(T)$  can be expressed as a function of temperature ( $T$ ) given by the equation:

$$G(T) = p_v(T) \left( \frac{M}{T} \right)^{1/2} \tag{6}$$

where  $p_v$  is the vapor pressure and  $M$  is the molecular weight of the material.

The vapor pressure above the surface is given by the Clausius–Clapeyron equation as [41, 42]:

$$p_v = p_0 \exp \left[ \frac{M \Delta H_v(T_b)}{k_b} \left( \frac{1}{T_b} - \frac{1}{T} \right) \right] \tag{7}$$

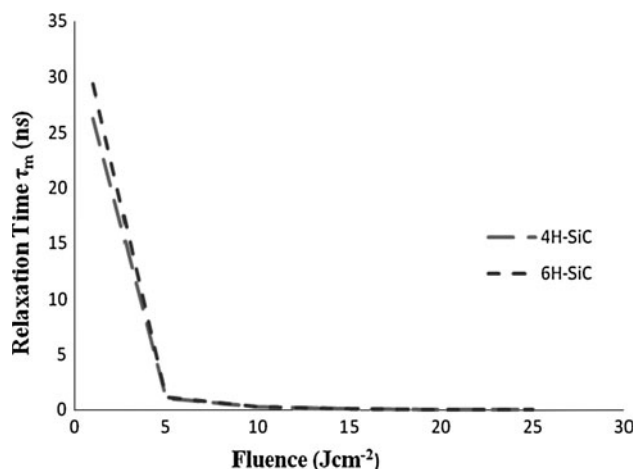


**Fig. 7** Relaxation time ( $\tau_m$ ) as a function of laser fluence for both SiC polytypes

where  $\Delta H_v(T_b)$  is the vaporization enthalpy at boiling temperature ( $T_b$ ),  $k_b$  is the Boltzmann constant, and  $p_0$  is atmospheric pressure taken as 1 atm. The value for enthalpy formation of Si was used as the vaporization enthalpy. The results were compared with experimental data as shown in Fig. 8. The model underestimates the experimental data for fluences ( $<5 \text{ J cm}^{-2}$ ) that could be due to the evaporation of carbon which was not considered in the analysis. At higher fluences, however, the experimental data was lower than that predicted by Eq. 6 which can be attributed to the development of a recoil pressure due to the evaporated material [34].

### Region 2 ( $5\text{--}15 \text{ J cm}^{-2}$ )

It has been reported that one of the underlying mechanisms causing ablation of semiconductors using nanosecond pulsed lasers is explosive boiling or phase explosion [34, 43–45]. Explosive boiling occurs when the surface temperature of the ablated material reaches its thermodynamic critical temperature value ( $T_c$ ). The critical temperature of SiC, however, is taken as 5000 K based on an ablation study of SiC with a 248 nm excimer laser [43]. The energy balance and heat transfer models indicate that at  $\sim 5 \text{ J cm}^{-2}$ , the decomposition products of SiC reach  $T_c$ . Explosive boiling occurs above this fluence range and drives the ablation in this region. Consequently, large vapor bubbles are formed in the superheated melt layer which receives large density fluctuations near the critical state ( $\sim 0.84 T_c$ ) [46, 47]. The rapid expansion of these vapor bubbles results in homogeneous nucleation that leads to the violent ejection of mass in the form of particulates that increases the ablation rate [48]. Estimates were made for the laser irradiances needed to induce explosive boiling in superheated liquid silicon using heat transfer model (Eq. 4).  $I_0$  was evaluated for  $T(x,t) = 0.84 T_c$ . The thermal

properties of silicon were taken from Refs. [49, 50]. The fluence was computed to be  $\sim 2 \text{ J cm}^{-2}$  which is less than the experimental value of  $\sim 5 \text{ J cm}^{-2}$ . The differences could be attributed to the negligence of carbon removal and the formation of plasma which absorbs a portion of laser energy incident on the target. Plasma effect can, however, be minimized by a shielding gas that has high ionization potential such as helium [51].

The thickness of melt layer can be approximated as equal to the critical radius ( $r_c$ ) of the vapor bubble at which it will explode as given by the expression [44, 52, 53]:

$$r_c = \frac{2\sigma}{p_v(T_1) \exp\{v_1[p_1 - p_v(T_1)]/R_v T_1\} - p_1} \quad (8)$$

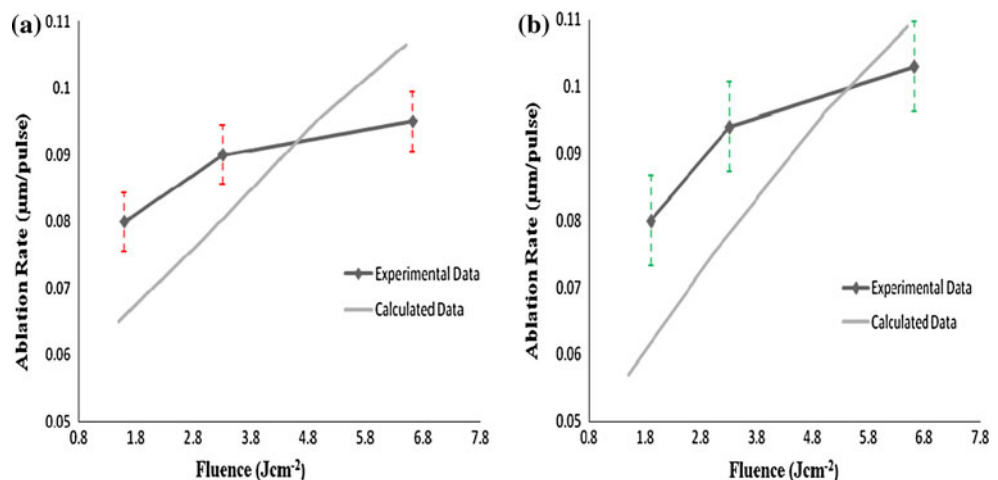
where  $\sigma$  is the surface tension that ranges from 0.14 to  $0.73 \text{ N m}^{-1}$  [44],  $v_1 = 1/\rho_1$  (density of superheated liquid),  $p_1$  is the pressure of liquid silicon layer approximated to be  $0.54 p_v$  [44],  $T_1$  is the temperature of superheated liquid approximated to be  $0.84 T_c$  [54, 55], and  $R_v$  is the gas constant.

The critical radius was estimated to be in the range of 2–10  $\mu\text{m}$  as shown in Fig. 9. The critical diameter of the bubble is much larger than the thermal penetration depth for silicon ( $\sim 2 \mu\text{m}$ ). Therefore, it can be inferred that the bubble cannot grow to its critical size during the laser pulse, and will burst preventing the homogeneous nucleation. It has been suggested that the vapor bubbles take a characteristic time ( $\tau_c$ ) to grow to the critical size ( $r_c$ ) [53, 56, 57]. The expression for  $\tau_c$  can be written as [57]:

$$\tau_c = r_c \left\{ \frac{2}{3} \left[ \frac{T_1 - T_{\text{sat}}(p_1)}{T_{\text{sat}}(p_1)} \right] \frac{L_{\text{ev}} \rho_v}{\rho_1} \right\}^{1/2} \quad (9)$$

where  $T_{\text{sat}}(p_1)$  is the saturation temperature at the superheated liquid pressure determined from Clausius–Clapeyron equation and  $L_{\text{ev}}$  is the latent heat of vaporization for silicon.

**Fig. 8** Comparison of experimental and calculated ablation rate in Region 1 for **a** 4H-SiC, **b** 6H-SiC



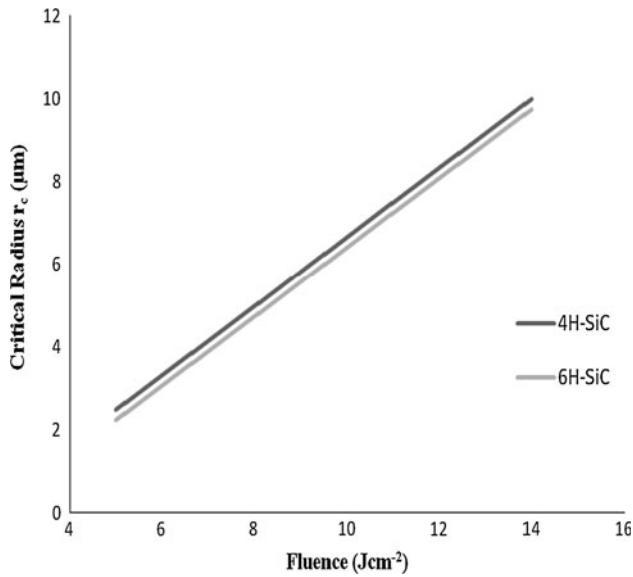


**Fig. 9** Critical radius as a function of fluence in Region 2 for both SiC

The characteristic time was estimated to be in the range of 150–500 ns. Assuming upper bound limit as the characteristic time delay (500 ns), it can be stated that the homogeneous nucleation can take place in Region 2 after ~20 pulses in this study. To validate our model, we approximate the experimental ablation rate based on the calculated results shown in Fig. 10. It can be observed that the ablation rates are still larger than the experimental data. This could be due to the underestimation of  $T_c$  and negligence of energy losses due to plasma shielding.

*Region 3 (15–25 J cm<sup>-2</sup>)*

It has been reported that at high laser power intensities (0.5–10 GW cm<sup>-2</sup>), which corresponds to the fluence range in Region 3, the surface temperature of the material

may still increase, however, its contribution to the ablation process is not so pronounced [58]. This supports our experimental data and temperature models. The impact of plasma shielding in this region is so large that a significant amount of laser energy is screened off from reaching the target surface. In fact, Chen and Bogaerts [59] reported that the fraction of laser energy absorbed by the plasma drastically increases from approximately 1–48%, with laser irradiance varying from 0.19 to 0.9 GW cm<sup>-2</sup>. The two dominant mechanisms for the absorption of laser light are: inverse Bremsstrahlung and photoionization of excited atoms [58–60]. A theoretical prediction of the degree of plasma absorption near this fluence range is, however, difficult due to computational complexities and lack of material properties.

Fabrication results

Figure 11a–d shows the profiles and striations of excimer laser micromachined trench measuring 1.5 × 0.5 mm (120 µm deep, approximately) in 6H-SiC using 85 mJ (7 J cm<sup>-2</sup>) at 10 Hz. The presence of recast layers along the sidewall and micro-cracks along the outer edge can be clearly seen. When removing large amount of material for deep structures, the debris re-deposition was very pronounced due to ejected material and re-condensed vapor that forms a loosely adhered film on the surface. SiC decomposes to Si and C at high temperatures and recombines to form highly volatile species as Si<sub>2</sub>C and SiC<sub>2</sub> [35]. Phase transition and/or repeated heating and cooling of this layer promotes cracking [61]. The fine debris field was found at a distance of 500–700 µm in some instances, and coarse debris was found to have formed near the machined areas. The presence of cracks, recast layers, and ripple patterns (discussed in the next section) illustrates adverse thermal damages associated with UV laser micromachining, and are attributed to vaporization and explosive

**Fig. 10** Comparison of experimental and calculated ablation rate in Region 2 for **a** 4H-SiC, **b** 6H-SiC

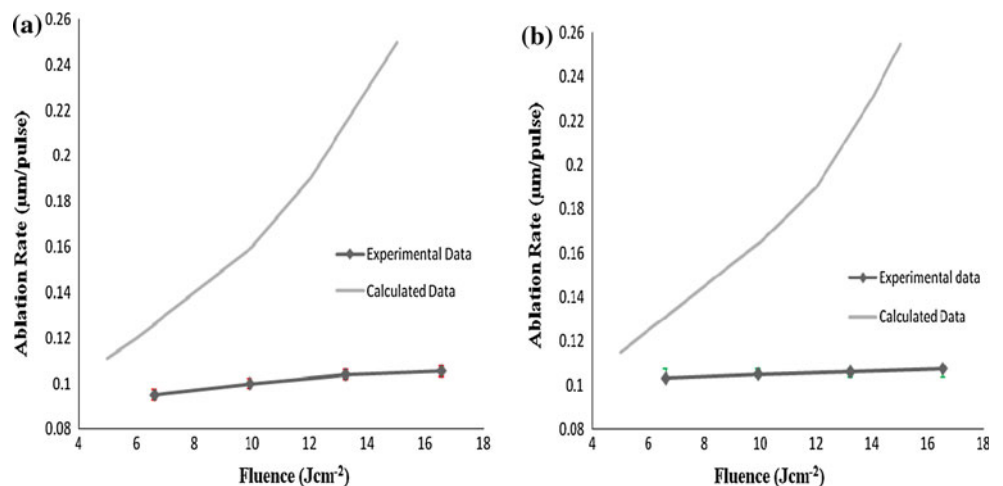
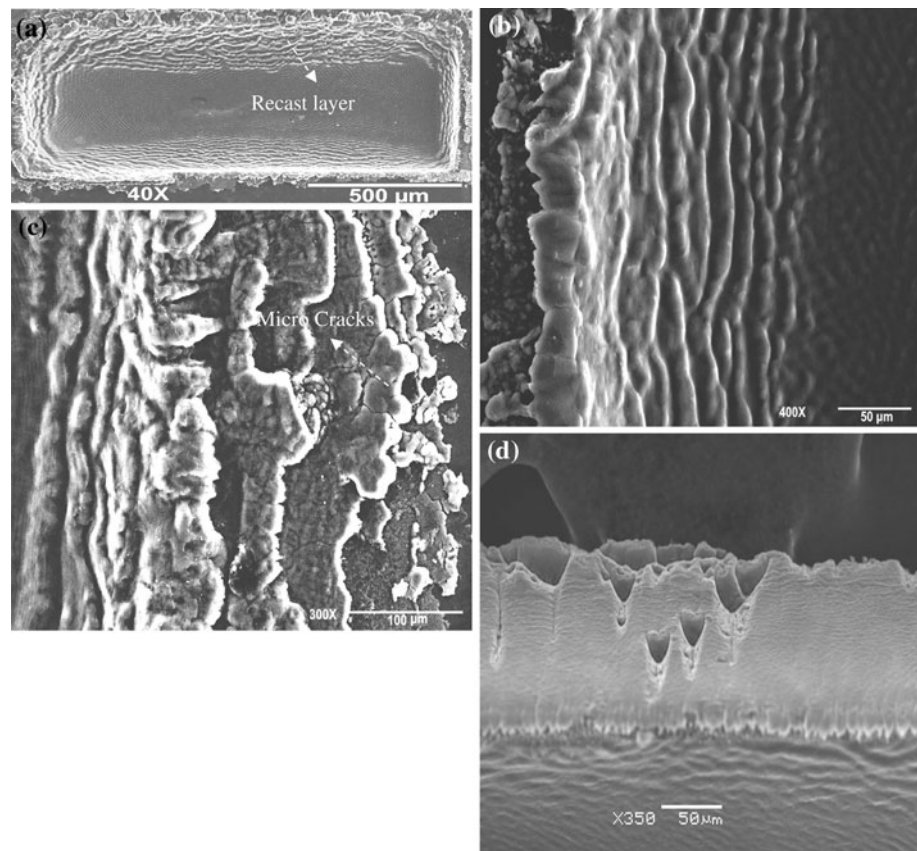




**Fig. 11** Excimer laser micromachined micro-trench in 6H-SiC showing **a** cross-sectional view, **b** sidewall, **c** micro-cracks along the outer edge, and **d** recast layers along the sidewall



boiling mechanisms. Post-processing such as chemical cleaning may become necessary to eliminate the loosely attached debris as shown in Fig. 12.

Figure 13 is the magnified view of the bottom regions of both SiC using  $7 \text{ J cm}^{-2}$  with 800 pulses at 10 Hz which display the presence of laser-induced surface structures (also called ripples). Many investigations have shown that laser irradiation over a broad range of wavelengths can create ripple patterns on many different semiconductors, metals, dielectrics, and polymers [62–67]. Based on these studies, such structures can be divided into two categories:

- (i) resonant periodic structures (RPS) that depend on the wavelength, polarization, and incidence angle of laser radiation [63, 66]. The periodicity can be calculated, with an accuracy of few percent, from Rayleigh's diffraction condition, as:

$$\Lambda = \frac{\lambda}{n_0[1 \pm \sin \theta]} \quad (10)$$

where  $n_0$  is the index of refraction of the incident medium, and  $\theta$  is the angle of incidence relative to the surface normal.

- (ii) non-resonant periodic structures (NRPS) that are neither related to the wavelength nor to the degree and direction of polarization of the incident

beam. NRPS was most probably reported for the first time by Bastow [67]. Structures with a period  $\Lambda \sim 10 \mu\text{m}$  were seen in the laser irradiation zone as a result of ruby laser pulses ( $\lambda = 0.694 \mu\text{m}$ ,  $\tau_p = 10 \text{ ns}$ ). More thorough investigations of NRPS have been reported in Refs. [68–70] using non-polarized radiation generated by  $\text{CO}_2$  laser sources ( $\tau_p = 1.7 \text{ ns}$ ), and in Ref. [71] using XeCl excimer laser ( $\lambda = 0.308 \mu\text{m}$ ,  $\tau_p = 30 \text{ ns}$ ). All of these studies reveal that these structures are independent of wavelength, target material, beam polarization, and details of surface roughness. The exact mechanism through which NRPS occur, however, is not yet fully understood.

The periodicity of ripple patterns observed in our study is of the order (5–10  $\mu\text{m}$ ) which is much larger than the wavelength used (0.248  $\mu\text{m}$ ), suggesting that NRPS is the operative mechanism. Recently, similar results were observed on SiC using a 248 nm excimer laser [43]. Ursu et al. [71] postulated that NRPS occurs due to the instabilities evolving at the plasma–target interface that cause self-organization of the melt. Other researchers have reported that the presence of a Si/SiO<sub>2</sub> interface in the excimer laser processed part is responsible for the observation of periodic structures [72, 73].

**Fig. 12** Micro-trench machined in 6H-SiC using 85 mJ at 10 Hz: **a** without post-processing, **b** with post-processing

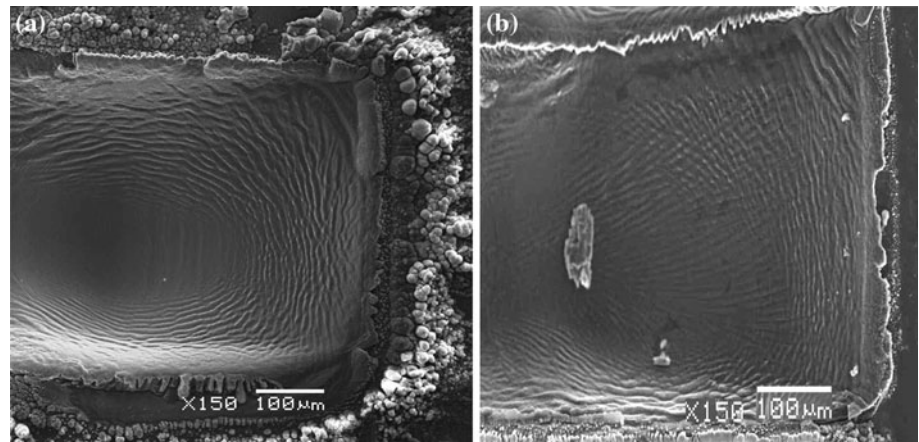
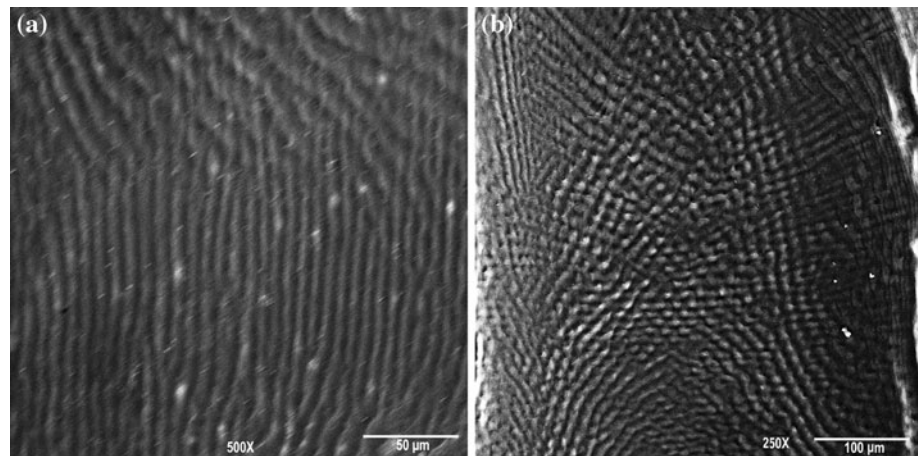


**Fig. 13** Bottom of a micromachined surface showing ripple patterns in **a** 4H-SiC, **b** 6H-SiC



## Conclusion

Pulsed laser ablation (at 248 nm) of single crystals of both 4H-SiC and 6H-SiC produced nearly identical ablation characteristics. The increase in ablation rate for energy fluences in the range  $0.5\text{--}1.25\text{ J cm}^{-2}$  was not pronounced unlike that of Si. Photothermal processes dominated the ablation in both polytypes. The ablation process began with the decomposition of SiC at fairly low fluences (ranging from  $1\text{--}1.25\text{ J cm}^{-2}$ ) and then at fluences in the range  $1.25\text{--}5\text{ J cm}^{-2}$  driven by vaporization of silicon and carbon species formed as a result of SiC decomposition. For fluences  $>5\text{ J cm}^{-2}$ , explosive boiling (or phase explosion) is believed to occur. At  $\sim 15\text{ J cm}^{-2}$ , the ablation rate reaches a saturation point due to extensive plasma shielding. No single model could explain the ablation behavior of both the polytypes (taking into account its thermodynamic and optical properties), and it is unlikely that such a model can be developed due to unavailability of their temperature-dependent properties and interplay of various mechanisms. To our knowledge, this is the first time that the ablation characteristics of single crystal 4H-SiC and 6H-SiC were compared over the wide range of fluence.

Micromachining of SiC with the excimer laser is accompanied by the formation of recast layers, micro-cracks, and ripple patterns. Post-processing improved the quality of machined features and minimized the thermal damage via chemical cleaning. Thus, excimer laser micromachining is a promising technology in fabricating high quality SiC structures.

**Acknowledgements** This material is based in part upon work supported by the National Science Foundation under Grant Number CMMI-0619115. Any opinions, findings, and conclusions or recommendations expressed in this material are those of the authors and do not necessarily reflect the views of the National Science Foundation.

## References

- Östling M, Koo SM, Zetterling CM, Khartsev S, Grishin A (2004) *Thin Solid Films* 469–470:444
- Dong Y, Zorman C, Molian P (2003) *J Micromech Microeng* 13:680
- Young DJ, Jiangang D, Zorman C, Ko WH (2004) *IEEE Sens J* 4:464
- Jepps NW, Page T (1983) In: Krishna P (ed) *Progress in crystal growth and characterization*. Pergamon Press, Oxford
- Méndez D, Aouni A, Araújo D, Bustarret E, Ferro G, Monteil Y (2005) *Mater Sci Forum* 483–485:555

6. Zhang J, Sugioka K, Wada S, Tashiro H, Toyoda K, Midorikawa K (1998) *Appl Surf Sci* 127–129:793
7. Mehregany M, Zorman C (1999) *Thin Solid Films* 355–356:518
8. Pearton SJ, Abernathy CR, Gila BP, Ren F, Zavada JM, Park YM (2004) *Solid State Electron* 48:827
9. Palma C, Sapia C (2000) *J Electron Mater* 29:607
10. Kim S, Bang BS, Ren F, D'Etremont J, Blumenfeld W, Cordock T, Pearson SJ (2004) *J Electron Mater* 33:477
11. Schlaf M, Sands D, Key PH (2000) *Appl Surf Sci* 154–155:83
12. Zekentes K, Zergioti I, Klini A, Constantindis G (2006) *Mater Sci Forum* 527–529:1119
13. Battula A, Theppakuttai S, Chen S (2006) *J Microlith Microfab Microsys* 5:011009-1
14. Zhang J, Sugioka K, Wada S, Tashiro H, Toyoda K (1997) *Appl Phys A* 64:367
15. Itoh N (1997) *Nucl Instrum Methods B* 122:405
16. Lambrecht WRL, Segall B, Suttrop W, Yoganathan M, Devaty RP, Choyke WJ, Edmond JA, Powell JA, Alouani M (1993) *Appl Phys Lett* 63:2747
17. Logothetidis S, Petalas J (1996) *J Appl Phys* 80:1768
18. Sridhara SG, Devaty RP, Choyke WJ (1998) *J Appl Phys* 84:2963
19. Blank TV, Goldberg YA, Kalinina EV, Konstantinov OV, Konstantinov AO, Hall'en A (2005) *Semicond Sci Technol* 20:710
20. Philipp HR, Taft EA (1960) In: O'Connor JR, Smiltens J (eds) *Silicon carbide—a high temperature semiconductor*. Pergamon Press, Oxford, London, New York, Paris
21. Levinshtein ME, Rumyantsev SL, Shur MS (2001) *Properties of advanced semiconductor materials*. Wiley, New York
22. Zetterling C-M (2002) *Process technology for silicon carbide*. INSPEC, London
23. Nilsson O, Mehling H, Horn R, Fricke J, Hofmann R, Muller SG, Eckstein R, Hofmann D (1997) *High Temp High Press* 29:73
24. Desbiens J-P, Masson P (2007) *Sens Actuators A* 136:554
25. Tseng AA, Chen Y-T, Ma K-J (2004) *Opt Lasers Eng* 41:827
26. Reitano R, Baeri P (1996) *Nucl Instrum Methods Phys Res B* 116:369
27. von der Linde D, Sokolowski-Tinten K, Bialkowski J (1997) *Appl Surf Sci* 109–110:1
28. McGeough J (2002) *Micromachining of engineering materials*. Marcel Dekker Inc., New York, Basel, pp 219–221
29. Furzikov NP (1990) *Appl Phys Lett* 56:1638
30. Carslaw HS, Jaeger JC (1959) *Conduction of heat in solids*, 2nd edn. Clarendon, Oxford
31. Von Allmen MF, Lau SS (1982) In: Poate JM, Mayer JW (eds) *Laser annealing of semiconductors*. Academic Press, New York
32. Ready JF (1971) *Effects of high-power laser radiation*. Academic Press, New York
33. Ozisik N (1993) *Heat conduction*. Wiley, New York
34. Yoo JH, Jeong SH, Greif R, Russo RE (2000) *J Appl Phys* 88:1638
35. Kim JJ, Katz DJ (1987) United States Patent 4649002, Kennecott Corporation, Ohio
36. Song Y, Smith FW (2002) *Appl Phys Lett* 81:3061
37. Duanming Z, Dan L, Zhihua L, Li G, Xinyu T, Li L, Ranran F, Dezhi H, Gaobin L (2007) *Appl Surf Sci* 253:6144
38. Dan L, Duanming Z (2008) *Chin Phys Lett* 25:1368
39. Gorelik T, Urban S, Falk F, Kaiser U, Glatzel U (2003) *Chem Phys Lett* 373:642
40. Savvatimskiy AI (2005) *Carbon* 43:1115
41. Bauerle D (2000) *Laser processing and chemistry*. Springer-Verlag, Berlin, New York
42. Amoroso S (1999) *Appl Phys A* 69:314
43. Neri F, Barreca F, Trusso S (2002) *Diam Relat Mater* 11:273
44. Yoo JH, Jeong SH, Mao XL, Greif R, Russo RE (2000) *Appl Phys Lett* 76:783
45. Craciun V, Bassim N, Singh RK, Craciun D, Hermann J, Boulmer-Leborgne C (2002) *Appl Surf Sci* 186:288
46. Martynyuk MM (1974) *Sov Phys Tech Phys* 19:793
47. Martynyuk MM (1976) *Sov Phys Tech Phys* 21:430
48. Song KH, Xu X (1998) *Appl Surf Sci* 127–129:111
49. Shanks HR, Maycock PD, Sidles PH, Danielson GC (1963) *Phys Rev* 130:1743
50. Glassbrenner CJ, Slack GA (1964) *Phys Rev* 134:A1058
51. Xing WH, Chen X (2003) *J Phys D Appl Phys* 36:2230
52. Reid RC (1976) *Am Sci* 64:146
53. Carey VP (1992) *Liquid–vapor phase phenomena*. Hemisphere, Washington
54. Miotello A, Kelly R (1999) *Appl Phys A* 69:S67
55. Kelly R, Miotello A (1996) *Appl Surf Sci* 96–98:205
56. Lu Q, Mao SS, Mao X, Russo RE (2002) *Appl Phys Lett* 80:3072
57. Russo RE, Mao XL, Liu HC, Yoo JH, Mao SS (1999) *Appl Phys A* 69 Suppl:S887
58. Bogaerts A, Chen ZY, Gizbels R, Vertes A (2003) *Spectrochim Acta B* 58:1867
59. Chen ZY, Bogaerts A (2005) *J Appl Phys* 97:063305
60. Lunney JG, Jordan R (1998) *Appl Surf Sci* 94:127
61. Islam MU, Mcgregor G, Campbell G (1992) United States Patent 5138130, National Research Council of Canada, California
62. Koo JC, Slusher RE (1976) *Appl Phys Lett* 28:614
63. Sipe JE, Young JF, Preston JS, Van Driel HM (1983) *Phys Rev B* 27:1155
64. McCulloch DJ, Brotherton SD (1995) *Appl Phys Lett* 66:2060
65. Dong Y, Molian P (2004) *Appl Phys Lett* 84:10
66. Wu XJ, Jia TQ, Zhao FL, Huang M, Xu NS, Kuroda H, Xu ZZ (2007) *Appl Phys A* 86:491
67. Bastow TJ (1969) *Nature* 222:1058
68. Aussenegg FR, Leitner A, Lippitsch ME (1983) *Surface studies with laser*. Springer Series in Chemical Physics, Berlin, Springer
69. Thomas SJ, Harrison RF, Figueira JF (1982) *Appl Phys Lett* 40:200
70. Caro RG, Gower MC (1982) *J Quant Electron QE*-18:1380
71. Ursu I, MihBilescu IN, Popa AL, Prokhorov AM, Ageev VP, Gorbunov AA, Konov VI (1985) *J Appl Phys* 58:3909
72. Yu JJ, Lu YF (2000) *Appl Surf Sci* 154–155:670
73. Giust GK, Simpson TW (1997) *Appl Phys Lett* 70:26